This manuscript was peer-reviewed and accepted by the editors prior to submission to Springer in December 2021 for publication as part of the Handbook for Space Resources.

Putzig, N.E., Morgan, G.A., Sizemore, H.G., Baker, D.M.H., Petersen, E.I., Pathare, A.V., Dundas, C.M., Bramson, A.M., Courville, S.W., Perry, M.R., Nerozzi, S., Bain, Z.M., Hoover, R.H., Campbell, B.A., Mastrogiuseppe, M., Mellon, M.T., Seu, R., Smith, I.B., in press. Ice Resource Mapping on Mars. Ch. 16 in Badescu, V., Zacny, K., Bar-Cohen, Y. (Eds.), Handbook of Space Resources, Springer Nature Switzerland AG.

Note that chapter numbering for this contribution is being recast from 18 to 16.

Abstract for Handbook of Space Resources Ch 18 Ice Resource Mapping on Mars

This chapter describes the rationale for considering shallowly buried (0 – > 5 m depth) water ice in the mid-latitude of Mars as a resource to support future human missions, and it describes a NASA-funded effort to map that ice with existing orbital remote-sensing data. In recent decades, numerous studies have used various data sets to investigate the presence and stability of water ice in the Martian shallow subsurface, with a view toward understanding the planet's recent climate history. As part of a renewed effort to prepare for human Mars missions, NASA has undertaken a more resource-focused approach. Here we describe the Mars Subsurface Water Ice Mapping (SWIM) Team's efforts to characterize the distribution of buried water ice resources across all longitudes from 60ºS to 60ºN latitude through the integration of multiple data sets. Deriving composite measures for the presence of accessible ice from a diverse range of remote sensing techniques with unique resolutions and caveats is a challenging problem. To enable data synthesis, the team developed a methodology that assigns values of ice consistency for mapped detections of hydrogen from a neutron spectrometer, thermal behavior from various thermal spectrometers, multiscale geomorphology from imagery and elevation data, and surface and subsurface echoes from a radar sounder. Faced with diverse sensing depths and footprints for these datasets, the team has been pursuing an optimal approach to best represent multi-dataset ice consistency. The current formulation includes the use of weighting factors tuned to depth zones of interest for resource extraction. In the absence of dedicated ground truth data, the validity of the team's efforts is assessed by comparing the maps to the locations of fresh, ice-exposing impacts. The highest ice-consistency values occur within discrete zones poleward of ~40º latitude, where ice is relatively shallow, but positive values extend well into the ~20º–30º latitude zone, which is preferable for landing sites due to engineering considerations.

18 Ice Resource Mapping on Mars

Nathaniel E. Putzig,[a,*] Gareth A. Morgan,[a,*] Hanna G. Sizemore,[a] David M. Hollibaugh Baker,[b] Eric I. Petersen,[c] Asmin V. Pathare,[a] Colin M. Dundas,[d] Ali M. Bramson,[e] Samuel W. Courville,[a,f] Matthew R. Perry,[a] Stefano Nerozzi,[g] Zachary M. Bain,[a] Rachael H. Hoover,[h] Bruce A. Campbell,[i] Marco Mastrogiuseppe,[j] Michael T. Mellon,[k] Roberto Seu,[j] Isaac B. Smith [a,l]

[a] Planetary Science Institute, [b] NASA Goddard Space Flight Center,
[c] University of Alaska - Fairbanks, [d] U.S. Geological Survey, [e] Purdue University,
[f] Arizona State University, [g] University of Arizona, [h] Southwest Research Institute,
[i] Smithsonian Institution, [j] Sapienza University of Rome, [k] Cornell University, [l] York University
* Joint first author

1.Ice as a Critical Resource for Human Missions

1.1.The Resource Value of Ice on Mars

In the effort to deliver humans to the surface of Mars and return them safely to Earth, current propulsion technology means that mass represents the ultimate premium for cost. Thus, any such endeavor is made much more feasible by leveraging all available in situ resources. The most valuable Martian resource for “living off the land” is water, which, when combined with atmospheric carbon dioxide, can provide methane as a fuel to sustain an outpost and for the return to Earth (Ash et al., 1978; Zubrin et al., 1991). Water also represents one of the most important ingredients of life support, including as a source of oxygen for breathing.

Mars has plentiful surface water ice, with multi-kilometer-thick ice caps in the form of the north and south polar layered deposits (NPLD/SPLD) and widespread shallow (< 1 m depth) ground ice in polar and subpolar regions. However, these sources of water are at latitudes that are not feasible for the initial human missions to the Red Planet. The higher solar radiation and corresponding manageable thermal environment and length of night offered by the lower latitudes are critical to mission success. In addition, low latitudes reduce energy needed for landing and launch from the surface for the return trip to Earth. Lower elevations are also desired, as they provide more atmosphere to slow down a spacecraft prior to a propulsive landing. Thus, locating the lowest-elevation, lowest-latitude sites that have significant water deposits is a key consideration in selecting future human landing sites on Mars.

1.2.Ice Stability on Mars

Numerical modeling of the stability of ground ice on Mars dates to the 1960s, when Leighton & Murray (1966) found that subsurface ice should be present in the higher latitudes, based on what was known at the time about Martian surface properties and temperature variations. Since that time, progressive improvements in our knowledge about those properties have been made, largely due to a series of ever-more-capable spacecraft in orbit and on the surface of Mars. The arrival of Mars Global Surveyor (MGS) and its Thermal Emission Spectrometer (TES) at Mars in the late 1990s (Christensen et al., 2001) precipitated a significant improvement in the accuracy and timespan of observations of temperatures and their variation over Martian seasons. Analyses of those variations allowed researchers to more accurately ascertain the stability and presence of current-day ice beneath a veneer of soil in high-latitude zones that extend

equatorward to about 50° latitude in each hemisphere (e.g., Mellon et al., 2004; Putzig & Mellon, 2007).

A few years into the MGS mission, the 2001 Mars Odyssey spacecraft arrived with the Mars Orbiter Neutron Spectrometer (MONS) onboard, allowing direct detection of hydrogen within the upper half meter of the subsurface. While lower concentrations of hydrogen likely indicate only hydrated minerals, in places where the fraction of hydrogen detected exceeds about 25%, the only plausible explanation is water ice (e.g., Feldman et al., 2002; Pathare et al., 2018). Thus, the neutron data provided confirmation of ground ice at high latitudes.

Subsequently, images from the High Resolution Imaging Science Experiment (HiRISE) camera and Compact Reconnaissance Imaging Spectrometer for Mars (CRISM) onboard the Mars Reconnaissance Orbiter (MRO) that arrived at Mars in 2006 have confirmed the presence of shallow, high-purity ground ice, not only at those higher latitudes but also extending down to a latitude of 39°N, via the discovery of new impact craters that expose and excavate ice within a meter of the surface (Byrne et al. 2009; Dundas et al. 2014; 2021). While the depths and latitudinal profiles observed by MONS and in the icy craters are broadly consistent with the general expectations based on theoretical models of stability, there are excursions of shallow ice extending closer to the equator than expected under current climate conditions. The existence of ice, out of equilibrium with the current climate, suggests the preservation of ice deposited in the mid-latitudes during previous climatic episodes has occurred. Mid-latitude remnant ice therefore represents an important resource for future missions.

2. The Mars Subsurface Water Ice Mapping (SWIM) Project

2.1. Project Overview

In 2015, NASA held a workshop in Houston, Texas, to begin consideration of landing sites for human missions to the surface of Mars. Workshop participants were instructed to evaluate 100-km-diameter exploration zones that would encompass the actual spacecraft landing site, human habitation facilities, features of scientific interest, and resources for generating fuel to sustain on-ground activities and supply an Earth-return vehicle. One outcome of the workshop was the realization that water, in the form of either hydrated minerals or buried water ice, represents an especially critical resource that had yet to be identified and assessed at the level needed to fully support landing-site planning. To address this need, NASA held a gathering of Mars scientists studying ice and hydrated minerals during the 2016 Fall American Geophysical Union Meeting in San Francisco to discuss the extent to which current data could help address knowledge gaps concerning water resources on Mars. The group identified a number of datasets and methods that would be useful for mapping hydrated minerals and buried mid-latitude ice, and NASA used this information to produce a request for proposals, issued in June 2017. After reviews, NASA selected and funded four proposals, two focused on the mapping of hydrated minerals and two on the mapping of buried water ice. The latter studies were limited to a swath of ~10° longitude in the Arcadia Planitia region, extending from the equator to 60°N, as NASA intended to evaluate the success of the ice-mapping methods proposed prior to broadening the study region (**Fig. 18.2.1**). These pilot studies, which began in late 2017 and early 2018, aimed to assess ice presence and map its distribution across the swath. Putzig et al. (2017) had proposed to use a combination of thermal data and modeling with radar observations of

subsurface interfaces, whereas Morgan & Campbell (2017) had proposed to use a combination of geomorphological data and radar observations of near-surface properties.

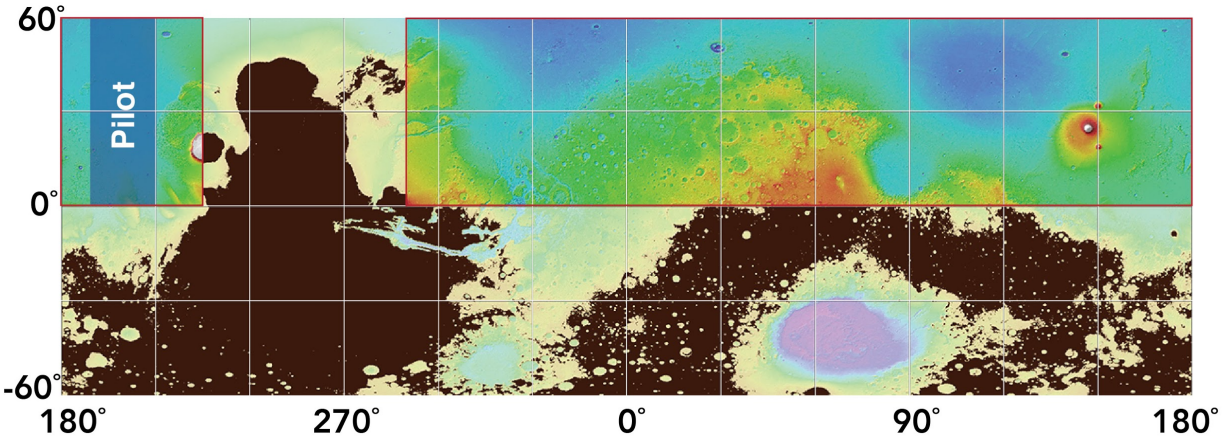

Figure 18.2.1. *Map of the SWIM study areas overlain above Martian topography. Blue box at 0°N to 60°N, 190°E to 210°E is the pilot study region. Red boxes in the northern hemisphere (-70°E to 225°E) delineate the 2019 study region. The remainder of the map is the 2020 study region, subject to cut-off at +1 km elevation (mask highlighted in black). MOLA basemap credit: NASA/JPL/USGS.*

Realizing the highly complementary nature of the two pilot studies, the teams proposed during a joint interim review at NASA Headquarters in July 2018 to merge their investigations in a larger study area. NASA agreed to the merger and to an expanded study area in a project extension entitled Subsurface Water Ice Mapping (SWIM) in the Northern Hemisphere of Mars (**Fig. 18.2.1**), which began in September 2018. For this first '2019' phase of the Mars SWIM project, we added additional techniques, including the use of neutron spectrometer data (**§18.2.2.1**), and we expanded the combined team to meet an increased workload under a seven-month timeline.

Our team began developing a means to present a coherent view of ice presence as informed by the collection of data and techniques, which we termed "ice consistency," *C*. For each technique, we came up with a means to evaluate how consistent each dataset at a given location is with either the absence or the presence of ice, assigning values between -1 (wholly inconsistent with ice) and +1 (wholly consistent with ice). To present an overall assessment of ice consistency with all relevant data, we introduced the SWIM Equation, wherein the technique-specific ice-consistency values are combined into a composite value for each map pixel. In the first SWIM phase, we chose to use a simple averaging, with each technique's ice consistency weighted equally with the others (**§18.2.3**). We presented results from the first study phase in a series of presentations at the 2019 Lunar and Planetary Science Conference in The Woodlands, Texas, and in a *Nature Astronomy* publication by Morgan et al. (2021).

Upon completion of the first SWIM study phase, NASA asked us to propose an extension to further refine our methods and expand the study to include all other areas below +1 km elevation and equatorward of 60° latitude in both hemispheres (**Fig. 18.2.1**). In this second '2020' phase of the Mars SWIM project, we made substantial refinements to our techniques, including the incorporation of a new thermal dataset and finer resolution geomorphic mapping (**§18.2.2**). In addition, we replaced the single SWIM Equation with a set of equations for three

distinct depth zones, weighting the terms in each equation by the sensing depths of the respective techniques. Realizing that this means of producing composite assessments of ice has some limitations, such as not allowing a quantitative treatment of uncertainties associated with each technique, we embarked on an exploration of an alternative presentation of our composite results through the use of Bayesian statistics (**§18.2.3**). Among other capabilities, this alternative approach allowed the team to consider ice presence in terms of probability, tunable for given depths or targeted concentrations of ice.

2.2.Spacecraft Datasets and Processing Techniques

2.2.1.Neutron Spectrometer Data

Our ice-consistency values derived from neutron spectroscopy are based on Mars Odyssey Neutron Spectrometer (MONS) observations of fast, thermal, and epithermal neutron fluxes at the top of the Martian atmosphere, which are highly sensitive to the presence of hydrogen (and, by extension, H_2O ice) within the upper half meter of the Martian subsurface (Feldman et al., 2002). We employed the global two-layer Water Equivalent Hydrogen (WEH) maps of Pathare et al. (2018), who refined the crossover approach of Feldman et al. (2011) to calculate the WEH abundances of an upper layer of weight fraction W_{up} with thickness D overlying a semi-infinite lower layer of weight fraction W_{dn}. For the SWIM project, we expressed the positive and negative ranges of neutron ice consistency $\boldsymbol{C_N}$ as linear functions of lower layer WEH abundance, W_{dn}:

$\boldsymbol{C_N = 1}$ ($W_{dn} \geq 25\%$) to $\boldsymbol{0}$ ($W_{dn} = 10\%$)
$\boldsymbol{C_N = 0}$ ($W_{dn} = 10\%$) to $\boldsymbol{-1}$ ($W_{dn} \leq 5\%$)

Maximum ($C_N = 1$) values were so assigned because $W_{dn} \geq 25\%$ corresponds to excess ice (i.e., the mass fraction needed to saturate the pore volume) for the surface density and porosity assumptions of Pathare et al. (2018). The other benchmarks ($C_N = 0$ at $W_{dn} = 10\%$, and $C_N = -1$ at $W_{dn} \leq 5\%$) were chosen based on our qualitative assessment of the likelihood of near-surface ice in all terrains exhibiting such W_{dn} values (see Fig. 11b of Pathare et al., 2018).

2.2.2.Thermal Datasets

Our thermal analysis combines three derived data products: two maps of surface-layer thermal inertia and ice-table depth independently produced by Bandfield & Feldman (2008) and Piqueux et al. (2019) as well as a global map of subsurface layering developed within the SWIM project using the methodology of Putzig & Mellon (2007). These three datasets (designated BF08, PQ19, and SP20, hereinafter) are built on the same core physics principle. Planetary surfaces consisting of different materials and different combinations of materials exhibit distinctive seasonal and diurnal variations in surface temperature and apparent thermal inertia (ATI) (Putzig & Mellon, 2007). Information about layering structure in the upper meter of the Martian subsurface can therefore be derived by forward-modeling the thermal behavior of a suite of material layering scenarios and comparing those model results to spacecraft observations of surface temperature or derived ATI. This section summarizes our methods and results, and a more detailed description is provided by Sizemore et al. (“Thermal analysis of the distribution of

shallow ice on Mars: Comparison of multiple datasets and methods for the SWIM Project," in prep.).

BF08, PQ19, and SP20 all employ this basic strategy to search for and map shallowly buried ice, but differ in terms of procedural details. Broadly, BF08 and SP20 apply somewhat different analysis pathways to the same spacecraft dataset, which is bolometric and surface temperatures from the Mars Global Surveyor (MGS) Thermal Emission Spectrometer (TES), whereas BF08 and PQ19 apply nearly identical analyses to two different datasets, temperatures from MGS TES and the Mars Reconnaissance Orbiter (MRO) Mars Climate Sounder (MCS), respectively.

Briefly, the BF08 and PQ19 approach is as follows: At each map pixel, a point in the orbit of Mars defined by a particular areocentric longitude of the Sun (L_S) designated L_S* is determined where modeled surface temperatures become the least sensitive to any putative buried ice. Surface-layer thermal inertia (TI) is then derived at L_S* using a standard lookup-table approach. Next, a suite of two-layer forward models are run at each pixel to predict the seasonal temperature variation resulting from ice occurring at a range of depths beneath a dry soil layer with thermal properties consistent with the previously derived TI. Spacecraft-observed surface temperatures are compared directly to modeled seasonal surface temperatures. The best match at each pixel is selected based on minimizing relative standard deviation (RSD), allowing the derivation of ice-table depth at locations where a match is identified (see Piqueux et al. (2019), Bandfield & Feldman (2008), and references therein for details).

A key characteristic of the BF08 and PQ19 approach is that all forward models include a lower layer with high thermal inertia, consistent with buried ice. Both BF08 and PQ19 used the KRC software package (Kieffer, 2013) for forward modeling. BF08 employed an older version that did not include temperature-dependent thermophysical properties whereas PQ19 employed a recent version that includes temperature dependence.

The SP20 ice-mapping process is based on the Putzig & Mellon (2007) approach of identifying a wide range of material heterogeneity types on the Martian surface. It uses global TES ATI maps computed at 10° intervals of L_S spanning a full Martian seasonal cycle. At each pixel of these maps, ATI is derived from TES bolometric temperatures using a lookup table of single-layer thermal-model results. A suite of two-layer thermal models is also run and used to derive ATI as a function of season via the same pathway used in the production of the global ATI maps. The suite of forward models includes layering scenarios with seven combinations of four material types defined by their thermal properties, including dust over sand (D/S), dust over duricrust (D/C), dust over rock (D/R), sand over rock (S/R), duricrust over dust (C/D), duricrust over sand (C/S), and rock over sand (R/S). Because the thermal properties of rock and ice are effectively equivalent, D/R and S/R scenarios are consistent with subsurface ice. We also consider D/C consistent with subsurface ice that does not completely fill the soil pore space, based on theoretical (Mellon et al., 1997; Piqueux & Christensen, 2009) and empirical (Siegler et al., 2012) models describing the increase of soil thermal conductivity with progressive cementation. A range of upper-layer thicknesses are allowed for each material combination in our two-layer model suite. The seasonal variation at each pixel of the global maps, ATI(L_S), is compared to the suite of forward models. Matches are identified based on minimizing RSD, and ice-table depth can be derived at locations of D/R, S/R, and D/C matches.

Our SP20 analysis used MARSTHERM (Putzig et al., 2013) for ATI derivation and forward modeling. This thermal model, which was originally developed for TES thermal inertia derivation (Mellon et al., 2000), includes a relatively sophisticated 13-layer one-dimensional radiative-convective atmospheric model (as compared to KRC's 1-layer radiative model). It does not include temperature dependence of thermal properties for surface and subsurface materials.

In the second SWIM phase, we modified the heterogeneity matching scheme from that of previous mapping efforts by Putzig & Mellon (2007), Putzig et al. (2014), and Morgan et al. (2021) to improve sensitivity to buried ice and derivation of ice-table depths. Specifically, we removed the shallowest depth nodes from the two-layer model suite to eliminate matches to models with extremely thin (< 1 mm) upper-layer duricrust, as we deemed these models to be physically implausible. We also updated the algorithm used for interpolating between discrete depth models to improve its accuracy.

BF08, PQ19, and SP20 all identified layering ostensibly consistent with ice at low latitudes. BF08 attributed this effect to atmospheric heat transport via Hadley circulation that is not accounted for in one-dimensional thermal models. They truncated their ice table maps equatorward of 50° in both hemispheres to compensate. PQ19 developed a more sophisticated (but still ad hoc) algorithm for latitudinally truncating their ice depth map where ice-table depths became shallower with decreasing latitude. They applied this algorithm equatorward of 50°N and 60°S, and they also removed outliers equatorward of 35° latitude.

In the SP20 analysis, we used a similar algorithm to truncate points where apparent ice detections were shallowing towards the equator in the BF08 and SP20 maps. We generated a filtered version of the SP20 map using a 9x9 pixel low-pass filter. Before filtering, we filled gaps in model matches by assuming that the empty pixel had the same ice depth as the next valid poleward pixel. We employed an equatorward-marching algorithm starting at 50° latitude in each hemisphere. If the local filtered pixel had an ice depth shallower than the median for that of the next five poleward pixels, we treated that pixel and all others equatorward of it as non-detections. We also applied a cutoff at 35° latitude to remove minor outliers. To facilitate comparisons, we applied a similar filter to the BF08 map, but using a 3x3 pixel filter and three poleward pixels due to the lower spatial resolution. Our approach produced reasonable agreement between the SP20 map and predictive ice stability maps by Mellon et al. (2004) in both hemispheres, and good agreement between the equatorward extent of ice in the SP20 and PQ19 maps of the northern hemisphere.

For all three maps, we computed thermal ice consistency $\boldsymbol{C_T}$ at each pixel where ice was modeled as a function of the predicted depth d to the ice table using the following scheme:

For d < 30 cm, $\boldsymbol{C_T = 1}$ (high consistency with ice)
For 30 cm ≤ d ≤ 50 cm, $\boldsymbol{C_T}$ decreases linearly from **1 to 0**
For all d > 50 cm, $\boldsymbol{C_T = 0}$ (data gives no information about the presence of ice)

We based this scheme on a suite of 1-, 2-, and 3-layer thermal models which show that it is increasingly difficult to distinguish icy and non-icy subsurfaces as ice-table depth increases beyond 30 cm (e.g., Fig. 1 of PQ19). We gave the three thermal ice-consistency maps (C_{BF08}, C_{PQ19}, and C_{SP20}) equal weighting in the combined map:

$$\boldsymbol{C_T} = (C_{BF08} + C_{PQ19} + C_{SP20}) / 3$$

Our choice to equally weight the three thermal ice-consistency maps does not indicate a preference for the TES data over the MCS data. Rather, it reflects the complexities and differing assumptions in the generation of all three maps from their constituent input data sources. A priori, none of the dataset–methodology combinations is to be preferred. In the absence of ground truth (at the multi-pixel scales), there is no clear rationale for weighting the maps differently.

2.2.3.Geomorphology

We determined our geomorphology ice-consistency values from previous and new mapping of periglacial and glacial features. Our new mapping included a grid-mapping survey of eight groups of landforms and terrain types that were inferred by previous workers to indicate the presence of ice (**Fig. 18.2.2**). These features included: mantle (Mustard et al., 2001; Milliken et al., 2003; Dundas et al., 2018), sublimation-type pits and textured terrain (Carr, 2001; Mangold, 2005; Kostama et al., 2006), scalloped terrain (e.g., Morgenstern et al., 2007), viscous flow features (VFF) (i.e., lobate debris aprons (LDA), lineated valley fill (LVF), concentric crater fill (CCF), and small-scale glacier-like forms (GLF)) (Milliken et al., 2003; Head et al., 2010; Souness & Hubbard, 2012; Levy et al., 2014), pedestal craters (Kadish et al., 2009), expanded craters (Viola et al., 2015), ring-mold craters (e.g., Kress & Head, 2008; Baker & Carter, 2019), and terraced craters (Bramson et al., 2015). We based our identification of landforms and descriptions on previous work, including recent grid-mapping efforts (see Ramsdale et al. (2017) and references therein). Maps produced by previous work were also used as input, including pedestal craters (Kadish et al., 2009; Viola & McEwen, 2018), LDA/LVF/CCF (Levy et al., 2014), expanded craters (Viola & McEwen, 2018), and scalloped terrain (Viola & McEwen, 2018).

In the first SWIM phase (mapping in the northern hemisphere between 0-225°E and 290-360°E longitude), we used a modified grid-mapping (Ramsdale et al., 2017) approach. Using a sampling of 4° x 4° MRO Context Camera (CTX) image mosaics within previously mapped geologic units (Tanaka et al., 2005), we tallied the number of observed periglacial and glacial landforms and extrapolated the observations to the mapped unit boundaries. The CTX mosaics we used are at 5 m/pixel resolution and are beta01 versions available from the Bruce Murray Laboratory for Planetary Visualization via http://murray-lab.caltech.edu/CTX/index.html (Dickson et al., 2018). We refined this approach in the second SWIM phase for our southern hemisphere mapping, surveying periglacial and glacial landforms using the CTX mosaic within 1° x 1° grid cells between 24°S and 38°S and within 4° x 4° cells elsewhere. For the 4° x 4° cells between 0°S and 24°S wherein we found positive identifications of glacial/periglacial landforms, we carried out additional grid mapping at the 1° x 1° resolution.

Using binary values (1=present, 0=absent), we marked observed landforms (from the list of eight above) regardless of their abundance within each grid cell. To compute geomorphology ice consistency $\boldsymbol{C_G}$, we tallied the number (n) of periglacial features (pf) identified within a given grid and weighted them based on their likelihood of containing ice. For most features, we assigned a weight of 0.1 per feature to indicate some ambiguity in their ice content. However, we chose higher weights for several features to reflect the high ice content required to maintain such features, including scalloped terrain (0.75), pedestal craters (0.75), and VFF (1). If the nominal C_G total for a given pixel was > 1, then we capped the pixel value at +1.

$$\boldsymbol{C_G} = \min [(\mathbf{0.1}*n_{pf1} + \mathbf{0.1}*n_{pf2} + \mathbf{0.1}*n_{pf3} + \ldots + \mathbf{0.75}*n_{scalloped} + \mathbf{0.75}*n_{pedestal} + \mathbf{1}*n_{VFF}), \mathbf{1}]$$

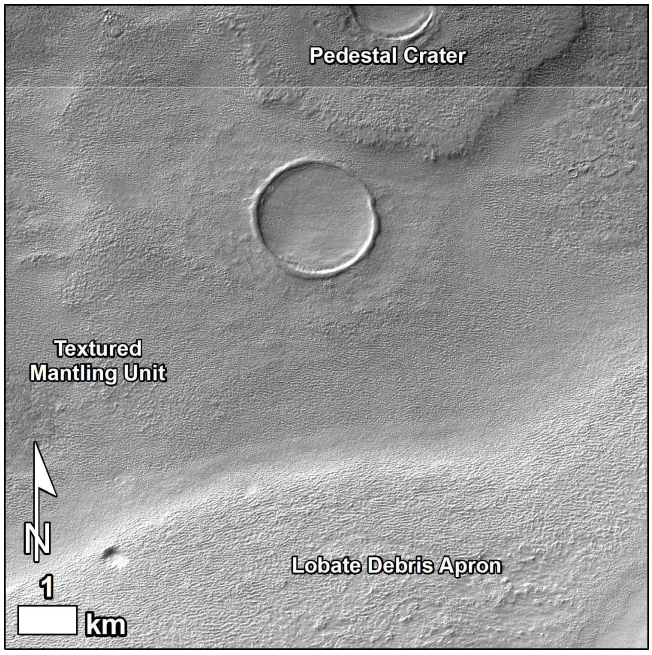

Figure 18.2.2. *Example of landforms mapped as part of the geomorphology analysis. In this example, the following features were tallied: textured terrain, mantle, LDA and pedestal crater. Image data, CTX mosaic centered at 44.07°S, 107.45°E*.

Final geomorphology ice-consistency values thus ranged from $C_G = 0$, i.e., no evidence of ice from periglacial/glacial features, to $C_G = 1$, i.e., highest evidence of ice from periglacial/glacial features. Note that values of $C_G < 0$ were not included in the geomorphology ice-consistency formulation since we did not specifically mark features that would be inconsistent with ice, for example exposed bedrock. In addition, to enable a layered approach, we split the geomorphology ice consistency into shallow (≤ 5 m) and deep (> 5 m) components, wherein mantled and textured terrains are limited to the shallow component C_{GS} and terraced craters are limited to the deep component C_{GD}. We included all mapped periglacial and glacial landforms in the shallow term due to the possibility that ice exists at depths ≤ 5 m for each of those landforms.

2.2.4.Radar Surface Power Analysis

The Shallow Radar (SHARAD) sounder onboard MRO was designed to search for subsurface structures by identifying radar-reflective interfaces ranging in depth from tens of meters to 1 km (or more) within the Martian crust (Seu et al., 2007). However, the radar echoes that are nominally from the surface also contain important information about materials within the upper ~5 m of the subsurface. The strength of the surface return is governed by multiple factors that include observational conditions (e.g., orientation of the spacecraft, state of the ionosphere), surface roughness, regional slope, and Fresnel reflectivity. The last of these can be estimated from the data by accounting for the others, and this technique provides a measure of near-surface density. Due to the low density of water ice relative to other geologic materials, measuring reflectivity offers a strategy to search for near-surface ice-rich deposits.

Broadly following a methodology first attempted with data from the Mars Advanced Radar for

Subsurface and Ionospheric Sounding (MARSIS) on Mars Express (Mouginot et al., 2010) while accounting for the higher frequency of SHARAD, we derived a process to isolate Fresnel reflectivity from the SHARAD dataset for the first SWIM phase (Morgan et al., 2021).

This process applies the following steps: (1) limit the ionosphere effects by excluding all daytime tracks, (2) normalize surface power for the effects of surface roughness using the SHARAD roughness parameter developed by Campbell et al. (2013) (**Fig. 18.2.3**), (3) correct the loss of power due to regional slope using the median slope value over a Fresnel zone (3 km) as derived from Mars Orbiter Laser Altimeter (MOLA) data, and (4) take the median value of all the corrected SHARAD returns sampled within a given region to account for MRO influences (spacecraft roll, solar-panel configuration) (see Grima et al., 2012).

After isolating an approximation of reflectivity from the MARSIS surface power measurements, Mouginot et al. (2010) took an additional step to convert their results to values of the real relative dielectric permittivity (ε'). The ε' of a given geologic substrate controls the speed of radar signals as they pass through the subsurface. Measurements of ε' can therefore be compared against laboratory and field measurements to constrain bulk subsurface compositions. In terms of the geologic materials that comprise the Martian subsurface, ε' is related to the density and porosity of those materials, and thus ice exhibits a much lower permittivity relative to basaltic lava flows. The radar subsurface analysis described in **§18.2.2.5** estimates the bulk ε' of the subsurface (to depths > 15 m) to search for low permittivity values that could indicate the presence of buried ice.

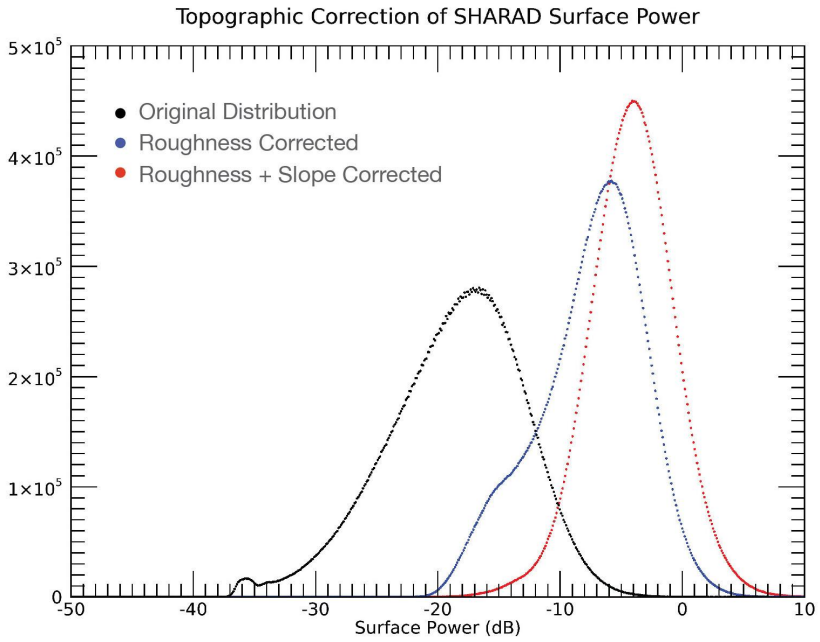

***Figure 18.2.3**. Corrections of the SHARAD surface return (60°S – 60°N) to isolate Fresnel reflectivity. The roughness correction (blue distribution) applied the Campbell et al. (2013) roughness parameter. The slope correction (red distribution) applied MOLA gridded data.*

For the radar surface analysis, we did not attempt to convert the corrected power returns to estimates of ε'. To achieve that would require calibration of the corrected power by comparing our measurements against terrains of a known permittivity. Mouginot et al. (2010) used the north and south polar layered deposits (NPLD and SPLD) as a reference for nearly pure water ice (ε' = 3.1, see Plaut et al., 2007; Grima et al., 2009). However, the shallow near-surface sampling of the SHARAD surface echo (~5 m) makes this approach problematic. In the case of the NPLD, the fine layering of the shallow subsurface can cause positive and negative interference of the SHARAD return whereas the surface of the SPLD is covered in a dust layer of variable thickness. As a consequence, the resulting SHARAD surface power returned over the polar caps is not equivalent to that of near pure ice and likely drifts from region to region in response to layering changes and variations in dust content.

In lieu of estimating values of ε', we opted to use the global distribution of corrected power values as a means to explore relative near-surface density. To test our approach, we compared the relationship between surface power and roughness exhibited by distinct Martian terrain types. Our analysis revealed that different units display similar curves, albeit with an offset in power. For example, high density terrains such as young volcanics were found to sit higher on the power axis relative to the icy polar caps (**Fig. 18.2.4**). To apply such an analysis across the SWIM study region, we translated the global power distribution such that surface power < -1σ maps to radar surface ice consistency C_{RS} **= +1**, surface power > 1σ maps to C_{RS} **= -1**, and surface power values of -0.5 σ, 0, and 0.5 σ were mapped to C_{RS} **= +0.5**, **0,** and **-0.5**, respectively.

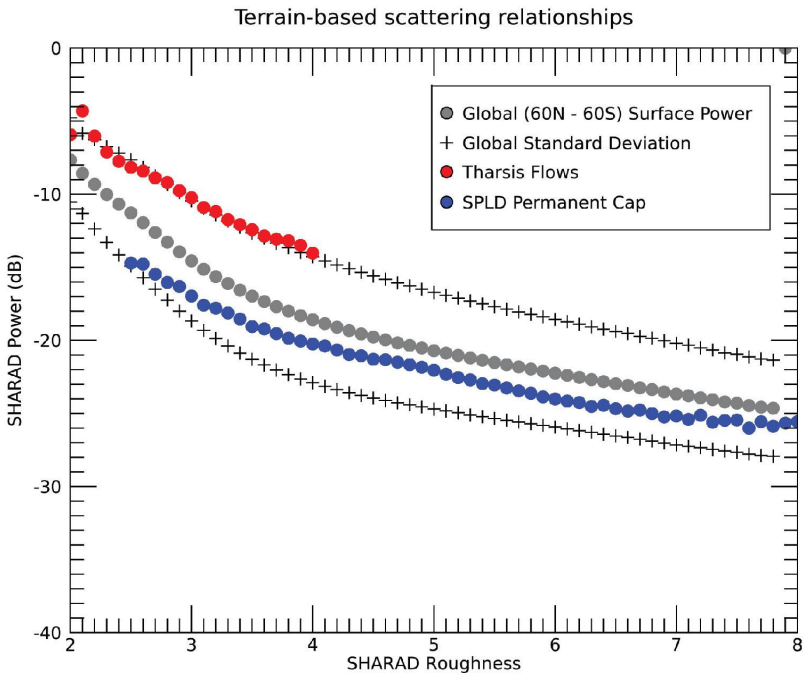

Figure 18.2.4*. Different Martian terrain types (CO_2 of the SPLD permanent cap in blue and basaltic substrate within Tharsis in red) exhibit similar radar scattering relationships (slopes in this figure) but distinct offsets in power. We attribute the power offset to differences of Fresnel reflectivity, where the higher-power terrain corresponds to a denser substrate relative to that of the lower-power terrain*.

2.2.5.Radar Subsurface Structure and Composition Analysis

We incorporated an analysis of subsurface radar returns observed by SHARAD into the SWIM project through an extensive mapping and interpretation effort undertaken by five members of the team who specialize in planetary radar sounding. For subsurface analysis, SHARAD data from a particular observing run along an MRO orbit segment are presented as images of returned radar power, with along-track distance on the horizontal axis and either delay time or depth on the vertical axis (a display format known as a radargram; see **Fig. 18.2.5**).

We visually inspected all available SHARAD radargrams in the SWIM survey regions to identify candidate subsurface signals. To assess the nature of candidate subsurface signals, we compared the radargrams to cluttergrams, which simulate the radar echoes produced by the Martian surface topography. Cluttergrams allow one to determine if the candidates are true subsurface signals or merely an artifact of off-nadir surface reflections returned to the spacecraft at delay times similar to those of potential subsurface returns (Choudhary et al., 2016). Upon determining that signals are likely to be true subsurface returns (i.e., not at the same locations and delay times as features in MOLA-derived cluttergrams), we then further analyzed them to estimate a value for the real relative dielectric permittivity (*ε'*) of the subsurface materials.

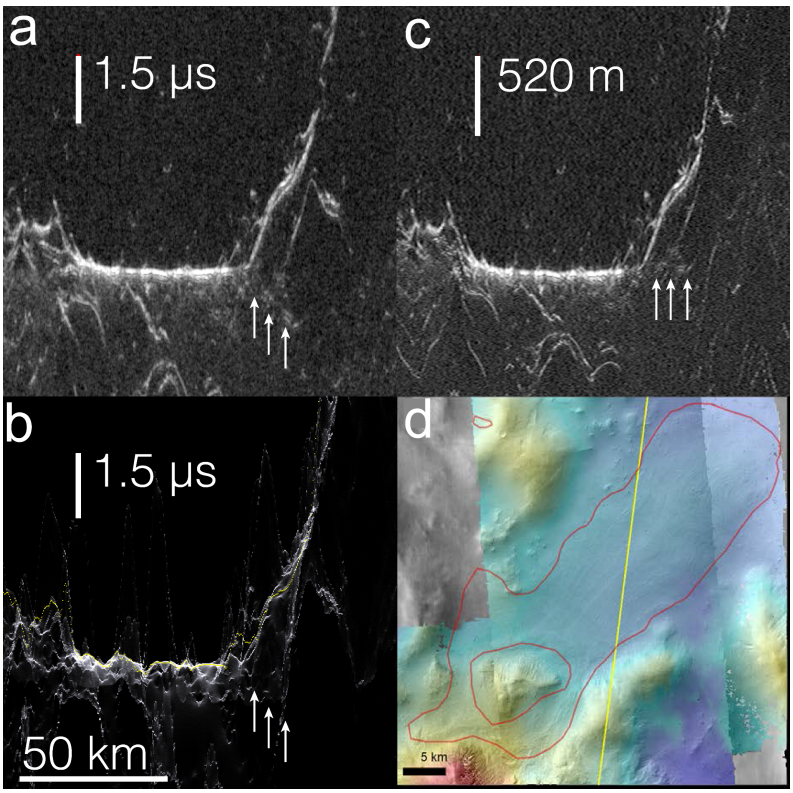

Figure 18.2.5*. SHARAD observation 35218-01 over an LDA in the southern hemisphere region of Argyre. (a) Delay-time radargram, with candidate subsurface signal indicated by white arrows. (b) Clutter simulation using a Mars Express High Resolution Stereo Camera digital terrain model, showing no predicted clutter at the delay time of the candidate signal. (c) Depth-corrected radargram using ε'=3; reflector has aligned with the surrounding plains. (d) Context image of radar ground track (yellow line) with topography and mapped extent of LDA (red line). After Berman et al. (2021).*

As is explained in **§18.2.2.4**, ε' controls the speed of radar signals as they pass through a geologic material, and thus places constraints on the subsurface composition. When the two-way delay time Δt is measured between SHARAD reflections bounding a geologic unit of known thickness h, ε' can be calculated as $\varepsilon' = (c\,\Delta t / 2h)^2$, where c = speed of light. Δt can be measured readily using SHARAD radargrams, but it is often more difficult to estimate h.

We estimated h using different methods appropriate for different types of geologic units. To enable quick application to many observations while producing reliable results in the aggregate, we optimized our techniques for each type of unit. For mantling units on the plains, we defined the base of the unit as a straight line between the plains elevation observed on either side of the unit in the radargram, with h being the depth to that line from the top of the unit. For geologic units that lie atop the plains but abut scarps and highlands on one side (such as for lobate debris aprons), we defined the base as a flat or fixed-slope interface continuous with the plains elevations observed on one side (following the methods of Petersen et al., 2018). In some special cases, we used stereo images to identify layer thickness in terraced craters, fossae, or other outcrops to provide point estimates of h. An important caveat is that the estimate of ε' is only as good as the estimate of h and the assumption that that thickness corresponds to the location of the interface producing the radar reflection.

Pure water ice has ε' ~3 (Ulaby et al., 1986) whereas basaltic materials typical of Martian bedrock have higher values of ε' ~6–12 (Campbell and Ulrichs, 1969). Mixtures produce ε' values that are intermediate between those of the individual materials. Mixing models (e.g., Sihvola, 1999; Stillman et al., 2010; Brouet et al. 2019) can predict ε' for mixed materials, but there remains an issue of non-uniqueness when translating from ε' to a specific composition.

Nevertheless, we used this knowledge of ε' values typical for our target ice deposits and Martian geology to formulate the following equation for radar subsurface (deep) ice consistency $\boldsymbol{C_{RD}}$:

$\boldsymbol{C_{RD}} = \mathbf{+1}$ where $\varepsilon' \leq 3$

$\boldsymbol{C_{RD}} = \mathbf{½\,(5 - \varepsilon')}$ where $3 \leq \varepsilon' \leq 7$ ($\boldsymbol{C_{RD}} = \mathbf{0}$ where $\varepsilon' = 5$)

$\boldsymbol{C_{RD}} = \mathbf{-1}$ where $\varepsilon' \geq 7$

In this framework, an ε' value of 3 is representative of pure ice, an ε' value of 7 is representative of pure basalt bedrock (no ice), and an intermediate ε' value is representative of an ice–rock mixture. While it is possible that materials such as high-porosity volcanic ash deposits could have a value of $\varepsilon' = 3$ while containing no ice, it is the combination of C_{RD} with ice-consistency values from the other instruments and techniques that help to disambiguate such materials.

2.3. Composite Ice Consistency from Data Integration

The greatest challenge to the SWIM project is synthesizing the diverse ice characterization techniques into congruent map products. As is outlined in **§18.2.2**, each of the five techniques provide contrasting perspectives of the physical properties of the subsurface, probe different depths, and exhibit separate caveats. The complexity of the problem is further compounded by the lack of ground-truth data that is sufficiently widespread to calibrate the individual techniques. For similar terrestrial problems, the integration of remote-sensing products typically is facilitated by the use of calibration maps produced through fieldwork. Remotely sensed datasets can then be calibrated via the ground-truth data. While a few very geographically limited areas, such as

the Phoenix landing site (Smith et al., 2008) and fresh ice-exposing impact craters (Byrne et al., 2009; Dundas et al. 2014; Dundas et al. 2021) provide actual and effective ground truth of buried ice on Mars, they are too few and far between to enable the production of calibration maps at the scales that would be required for the SWIM study's remote-sensing datasets.

Below, we describe two different approaches to integrating our ice characterization techniques. The first represents the evolution of the SWIM Equation derived for the first SWIM phase in the northern hemisphere (Morgan et al., 2021). The second introduces a Bayesian framework to synthesize the probabilistic range of ice content measured by each technique.

2.3.1. The SWIM Equations

The driving motivation behind our integration efforts is to track agreements between our diverse ice characterization techniques. Within this framework, ice consistencies derived from multiple data sources are valued above that from a single methodology. There is clearly a higher potential for ice in areas where more datasets are consistent with the presence of ice and fewer are inconsistent with ice. The SWIM equations were developed to rank locations across Mars based on both the number of ice signatures and the relative strength of those signatures. For the first SWIM phase, we applied a straightforward approach that averaged the five ice-consistency values into a single value of composite ice consistency (C_i):

$$C_i = (C_N + C_T + C_G + C_{RS} + C_{RD}) / 5 \qquad \text{(Eq. 1)}$$

As is the case for the individual techniques, C_i can in principle range from -1 (all techniques are fully inconsistent with the presence of ice) to +1 (all techniques are fully consistent with the presence of ice). A value of 0 reflects no data or a balanced ambivalence among the ice-characterization techniques. However, in our current implementation, ice consistency for our thermal and geomorphological techniques is restricted to the range of 0 to 1, and thus the minimum C_i value is limited -⅗.

To interpret our C_i results for landing-site planning, we consider a value corresponding to 1/(no. of techniques) = 0.2 as the minimum threshold for areas of interest that are likely to contain ice in quantities viable as a resource. The rationale behind this threshold assignment is that either one technique must post the maximum ice-consistency value while the others are inconclusive or multiple datasets must provide positive indications of ice. Following this same logic, we consider values of $C_i > 0.6$ to be of the highest significance, as this would indicate a majority of techniques are strongly supportive of ice.

The known locations of mid-latitude ice, as exposed by impacts (Byrne et al., 2009; Dundas et al., 2014) and along scarps (Dundas et al., 2018), are not statistically sufficient to warrant calibration of the individual terms. Consequently, our first approach was to treat all of the terms within the SWIM equation equally. Nevertheless, the ice-exposing impacts do provide an opportunity to assess the effectiveness of our mapping approach. For example, the SWIM region from the first phase of mapping (**Fig. 18.2.1**) contains 13 ice-exposing impact sites. The average C_i value for these sites is 0.26 ± 0.16 (Morgan et al., 2021), which is above our minimum threshold, lending confidence to our methodology. Another motivation we had for the absence of weighting in Eq. 1 for the first SWIM phase was to encourage community engagement and permit SWIM product users to experiment with different formulations to produce their own integrated maps.

During the second SWIM phase, we continued to develop our data integration techniques, encouraged by community feedback that suggested we examine alternative approaches. As the datasets behind the various techniques probe different depths into the subsurface, we chose to leverage those depth sensitivities to produce three new equations that correspond to three depth zones: < 1 m, which is dominated by neutron and thermal spectrometer data; 1–5 m, which is dominated by shallow geomorphic and radar surface-return data; and > 5 m, which is dominated by deeper geomorphic data and radar subsurface dielectric permittivity estimations. To enable this layered approach, we divided the mapped geomorphic landforms into two groups corresponding to ice presence above and below a depth of 5 m, as described in **§18.2.2.3**. In addition, we introduce weighting factors s_M, i.e., the shallowness of method M, which is determined by dividing the depth of interest for each equation by the sensing depth of each method. Thus, for the first depth zone at < 1 m, we have:

$$C_i\,[< 1\text{ m}] = (s_N C_N + s_T C_T + s_{GS} C_{GS} + s_{RS} C_{RS}) / (s_N + s_T + s_{GS} + s_{RS}) \quad \text{(Eq. 2)}$$

$$= (C_N + C_T + 0.2{*}C_{GS} + 0.2{*}C_{RS}) / 2.4$$

where s_N and s_T are both set equal to 1 because the neutron and thermal sensing depths of ~1 m are entirely within the zone of interest whereas s_{GS} and s_{RS} are both set equal to 0.2 because only 20% of the shallow-geomorphic and radar-surface sensing depths of ~5 m extend into the zone of interest. The deep radar consistency C_{RD} does not appear in the Eq. 2 because the *minimum* sensing depth (taken as the SHARAD range resolution) of ~15 m translates to an s_{RD} for this zone of 1/15 that makes any C_{RD} term negligible.

For the second depth zone at 1–5 m, we have:

$$C_i\,[1\text{–}5\text{ m}] = (s_{GS} C_{GS} + s_{RS} C_{RS} + s_{RD} C_{RD}) / (s_{GS} + s_{RS} + s_{RD}) \quad \text{(Eq. 3)}$$

$$= (C_{GS} + C_{RS} + 0.3{*}C_{RD}) / 2.3$$

where s_{GS} and s_{RS} are both set equal to 1 because the shallow-geomorphic and radar-surface sensing depths of ~5 m are entirely within the zone of interest whereas s_{RD} is set equal to 0.3 because only 30% of a nominal radar-subsurface sensing depth (taken as the SHARAD range resolution) of ~15 m extends into the zone of interest.

For the third depth zone at > 5 m, we have:

$$C_i\,[> 5\text{ m}] = (s_{GD} C_{GD} + s_{RD} C_{RD}) / (s_{GD} + s_{RD})$$
(Eq. 4)

$$= (C_{GD} + C_{RD}) / 2.0$$

where s_{GD} and s_{RD} are both set equal to 1 because the deep-geomorphic and radar-subsurface sensing depths extend indefinitely into the zone of interest.

Our formulation of the SWIM equations is by no means the only approach possible, and other methods may be brought to bear, depending on different goals of end users of the ice-consistency mapping products.

2.3.2.Bayesian Statistical Analysis

The SWIM equation approach to mapping ice consistency has two limitations: the values of ice consistency do not indicate ice concentration and there is no formal way to estimate uncertainty. A potential solution to these shortcomings is the use of Bayesian inversion. At the core of the SWIM project is an inverse problem wherein we have a set of satellite remote sensing data and we want to know the Martian subsurface composition that produces the measurements and whether that composition includes water ice. Bayesian inversion, as described by Tarantola (2005), is a well-developed procedure to solve inverse problems. Our application of the Bayesian procedure is based on the ability to represent the likelihood of all possible subsurface compositions as a probability density function (PDF). To formulate that function, we assume that the Martian subsurface is composed of ice, rock, and pore space. Thus, the set of all possible subsurface models can be described by two values: the volume percent of water ice and the volume percent of rock (with the pore volume given by the remaining percentage). In the absence of data or prior information, all composition models are equally likely. Our purpose in using the Bayesian method is to combine multiple sets of data to whittle down the set of possible model solutions and constrain the set of possible subsurface compositions at each location on Mars. Additionally, because the Bayesian approach is based on PDFs, the approach allows for the incorporation of measurement uncertainty.

Although some measurements may be ambiguous toward water ice, all the datasets we use allow us to place constraints on the composition of subsurface materials. For example, a low permittivity determined from radar reflections could either indicate water ice or highly porous material, but not solid rock. Conversely, a high thermal inertia determined from temperature measurements would suggest either solid rock or the presence of water ice, but not a porous material. Separately, the two measurements do not uniquely indicate ice, but together they do. Bayesian inversion allows us to handle such nuanced cases by probabilistically expressing the subsurface compositions that can explain each measured property.

We discretize the space of all composition models and link each model to potential data measurements via theoretical or empirical formulas. Radar reflections from the SHARAD instrument result in estimates of the subsurface dielectric permittivity. By simplifying the Maxwell Garnett mixing model (Koledintseva et al., 2006), we can express the effective permittivity ϵ_{eff} as a function of the subsurface composition as:

$$\epsilon_{eff} = \frac{\epsilon_r}{1 - f_i \frac{\epsilon_i - \epsilon_r}{\epsilon_i} - f_p \frac{\epsilon_p - \epsilon_r}{\epsilon_p}},$$

where ϵ_i, ϵ_r, and ϵ_p are the permittivities of water ice, rock, and pore space, respectively, and f_i and f_p are the volume fractions of water ice and pore space, respectively. In reality, all types of rock do not have the same permittivity, so we assign ϵ_r to a distribution of values covering the range of plausible rock types on Mars. This means that rather than a given composition model mapping to one ϵ_{eff}, it maps to a distribution of ϵ_{eff} values. Likewise, a given estimation of ϵ_{eff} maps to a distribution of composition models.

The water equivalent hydrogen (WEH) values derived from MONS data by Pathare et al. (2018) can be expressed as a function of the subsurface composition:

$$WEH\% = \frac{M_i + M_h\, WEH_{hmax}}{M_{total}} \times 100\%$$

where water ice mass M_i = f_i x ρ_i is the water ice volume fraction f_i multiplied by the water ice density ρ_i (= 920 kg/m^3), hydrated mineral mass M_h = f_h x ρ_h is the hydrated mineral volume fraction f_h multiplied by the density of hydrated minerals ρ_h (≈ 1680 kg/m^3), WEH_{hmax}= 50% is the assumed maximum WEH% that could be recorded by a subsurface composed entirely of hydrated minerals, and the total mass M_{total} = M_i + M_h + M_{rock} + M_{air} . The density of the rock and the fraction of the rock that is composed of hydrated minerals are assigned to a distribution of values, so a given subsurface composition model maps to a distribution of WEH% values.

Analysis of TES data provides an estimate of the thermal inertia of the subsurface. The thermal inertia is related to the subsurface composition by:

$$TI = \sqrt{k\rho c_h}$$

where k is the thermal conductivity of the subsurface, ρ is the density of the subsurface, and c_h is the heat capacity of the subsurface. The densities and heat capacities are simply the volume-fraction weighted averages of the rock, ice, and pore space components, but the thermal conductivity is more nuanced. We use the approach described by Mellon et al. (1997) to write the thermal conductivity as a function of ice, rock, and pore-space composition. Following the rules outlined by Tarantola (2005), the set of theoretical relationships among datasets from the radar, neutron spectrometer, and thermal spectrometer can be used to create PDFs that relate a given measurement to a distribution of composition models.

Geomorphological features do not have strict mathematical relationships to water-ice content. However, geomorphology can be added to the Bayesian approach if treated as prior knowledge. For example, recent impact events in some regions of Mars expose water ice in and around the craters they form. Although the exact concentration of the ice may not be determined from images, the fact that ice is visible adds a constraint to the minimum amount of ice that must be present in the subsurface in the general vicinity of the crater (Dundas & Byrne, 2010; Dundas et al., 2014). Thus, we can assign qualitatively justified PDFs for all geomorphological features that are related to ice.

Once a PDF has been created for each dataset, we can combine the PDFs in a similar fashion to combining consistency values. For the near surface, 0–5 m depth, we combine PDFs for the geomorphology, radar surface data, thermal data, and neutron data. For the deeper subsurface, >5 m depth, we combine PDFs for the geomorphology and radar subsurface data. We combine the PDFs through multiplication, following the rules of Tarantola (2005). By definition, multiplying PDFs results in a new PDF that is always a more refined state of information. **Figure 18.2.6** shows an example combination of PDFs for the 0–5 m depth zone at one hypothetical location on Mars. The result gives us a PDF that indicates the most likely ice volume percent and also

how certain that value is. By repeating this process for every location on Mars, we can generate a probability map of water ice content across the Martian globe.

The Bayesian approach provides multiple advantages over the ice-consistency approach. First, it allows us to estimate ice percentage versus simply whether ice may or may not be present. Second, the method allows us to address quantitatively how measurement uncertainty and interpretation ambiguity lead to uncertainty of the ice concentration. Lastly, the procedure provides a robust set of rules for how to incorporate each element of knowledge we have about water ice on Mars. New data and information can easily be included into the framework to provide updated probability results, and by definition, new information can only refine the results and further constrain the composition. However, the SWIM Bayesian approach is still an area of active research that needs refinement and testing before the results are formally used. Specifically, we plan to refine the approach by adding compositional variation with depth to the models and by adding the correct depth dependence to each theoretical relation between measurement and composition when funding allows.

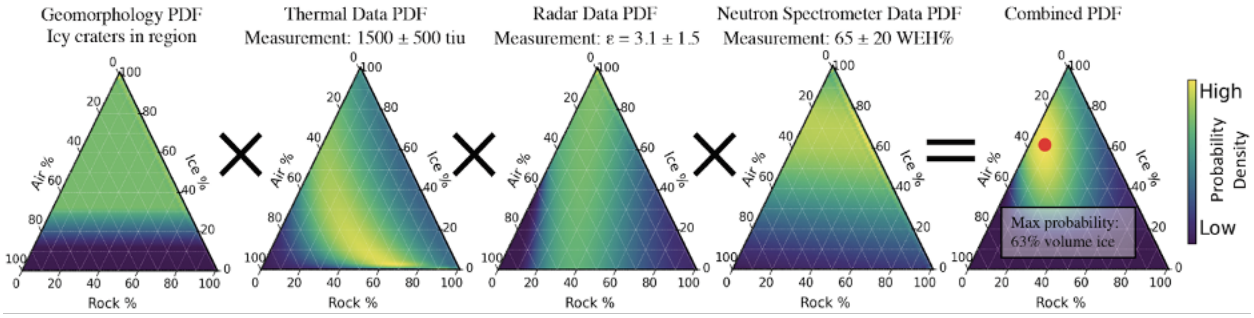

Figure 18.2.6. *Illustration of the Bayesian SWIM method applied for a single location on Mars that is in the vicinity of an icy crater and has a thermal inertia of 1500 ± 500 tiu, an effective permittivity of 3.1 ± 1.5, and a WEH of 65 ± 20%. Each observation and measurement has a PDF relating it to a set of permissible composition models. Upon multiplying the PDFs together, the result is a more limited set of models that can explain all measurements and indicates the most likely ice volume percentage (the red dot). In this case, the most likely concentration of water ice is 63%, and the overall result is consistent with porous dusty ice.*

3.SWIM Results

3.1.Non-layered Ice Consistency

We present the results of our predicted composite ice consistency (Eq. 1) in **Figure 18.3.1a**. In addition to extending the mapping beyond the northern hemisphere study area (Morgan et al., 2021), we revised the methods used in generating the dataset-specific ice-consistency maps as described in **§18.2.2**. This product provides an overall view of where the collection of datasets points toward a high likelihood of finding buried ice. However, it does not provide a clear sense of the distribution of that ice with depth nor of its concentration relative to other materials in the subsurface.

3.2.Ice Consistency for Depths less than 1 meter

We present the results of our predicted ice consistency for the upper meter of the Martian surface in **Fig. 18.3.1b**. Ice consistency in this depth range is driven by the weighted averages of the consistencies with ice from neutron and thermal spectrometers, surface radar, and shallow geomorphology observations (Eq. 2). Not surprisingly, the results are broadly consistent with those of prior mapping efforts based on data from thermal and neutron spectrometers, which are the dominant components of Eq. 2. To apply the SWIM 1.0 approach for determining the minimum threshold of an area of interest — 1/(no. of techniques) (Morgan et al., 2021) — we need to also factor in the weighting incorporated within Eq. 2 when designating the denominator. For C_i [< 1m], this equates to 1/2.4 = 0.42. In this case, either one technique (with a maximum weighting of 1) is recording a maximum positive ice consistency and the others are uncertain or, alternatively, multiple techniques are providing positive ice-consistency values. Considering this threshold of 0.42, we find that substantially high ice consistency occurs in three regions between 40° and 45° latitudes, specifically in Arcadia Planitia (170-220°E) and eastern Utopia Planitia (120–160°E) in the north and Promethei Terra (100–140°E) in the south. Also apparent in **Fig. 18.3.1b** are regions of slightly positive ice consistency ranging between 0.1 and 0.3 at low latitudes in Arabia Terra (0°E–50°E), Aeolis Mensae (165°E–200°E), and Medusae Fossae (165°E–200°E). Two analyses of epithermal-neutron flux — one using MONS data (Wilson et al., 2018) and one using Fine Resolution Epithermal Neutron Detector (FREND) data (Malakhov et al., 2020) — modeled a simplified uniform surface layer and argued for the presence of excess ice “oases” in these near-equatorial regions. However, Pathare et al. (2018) modeled a more realistic two-layer near surface that was constrained by epithermal, thermal, and fast neutrons, and they concluded that the MONS data are much more consistent with the widespread presence of hydrated minerals in these low-latitude regions. This conclusion is supported by a lack of highly elevated abundances of observed atmospheric water vapor that should result from the sublimation of such shallow excess ice at equatorial temperatures.

3.3.Ice Consistency for Depths of 1 to 5 meters

We present the results of our predicted ice consistency for depths between 1 and 5 m in **Fig. 18.3.1c**. Ice consistency in this depth range is driven by the weighted averages of the consistencies with ice from surface radar, deep radar, and shallow geomorphology observations (Eq. 3). The neutron and thermal spectrometer ice-consistency values are not included, as their measurements do not extend into this depth range. Compared with results for the top 1 m of the subsurface (**Fig. 18.3.1b**), the results for 1–5 m depths show a substantial equatorward expansion of areas containing evidence of ice, with moderate ice-consistency values extending to < 30° latitude in some locations, most notably in Arabia Terra south of Deuteronilus Mensae (10–60°E) and within the Hellas basin (~45°–90°E). The equatorward extent of continuous C_i [1–5 m] in both the northern and southern hemispheres is largely driven by the spatial occurrence of mantling units, which are included in the shallow geomorphology term (C_{GS}). The highest values of C_i [1–5 m] are in localized regions dispersed throughout Arcadia Planitia and the broader northern plains and in association with locations that have a high density of glacial features (LDA, LVF, and CCF) such as Deuteronilus Mensae and eastern Hellas. Intriguingly, several locations near the equator show low to moderate C_i [1–5 m]. Many of these locations are associated with the Medusae Fossae Formation, where pedestal craters are observed and where layers of dust might be contributing to the surface-radar signal. Near Schiaparelli crater in western Terra Sabaea (~5-10°S, 15°E), we mapped a number of landforms resembling CCF and other glacial features, consistent with previous work in this area (Shean, 2010).

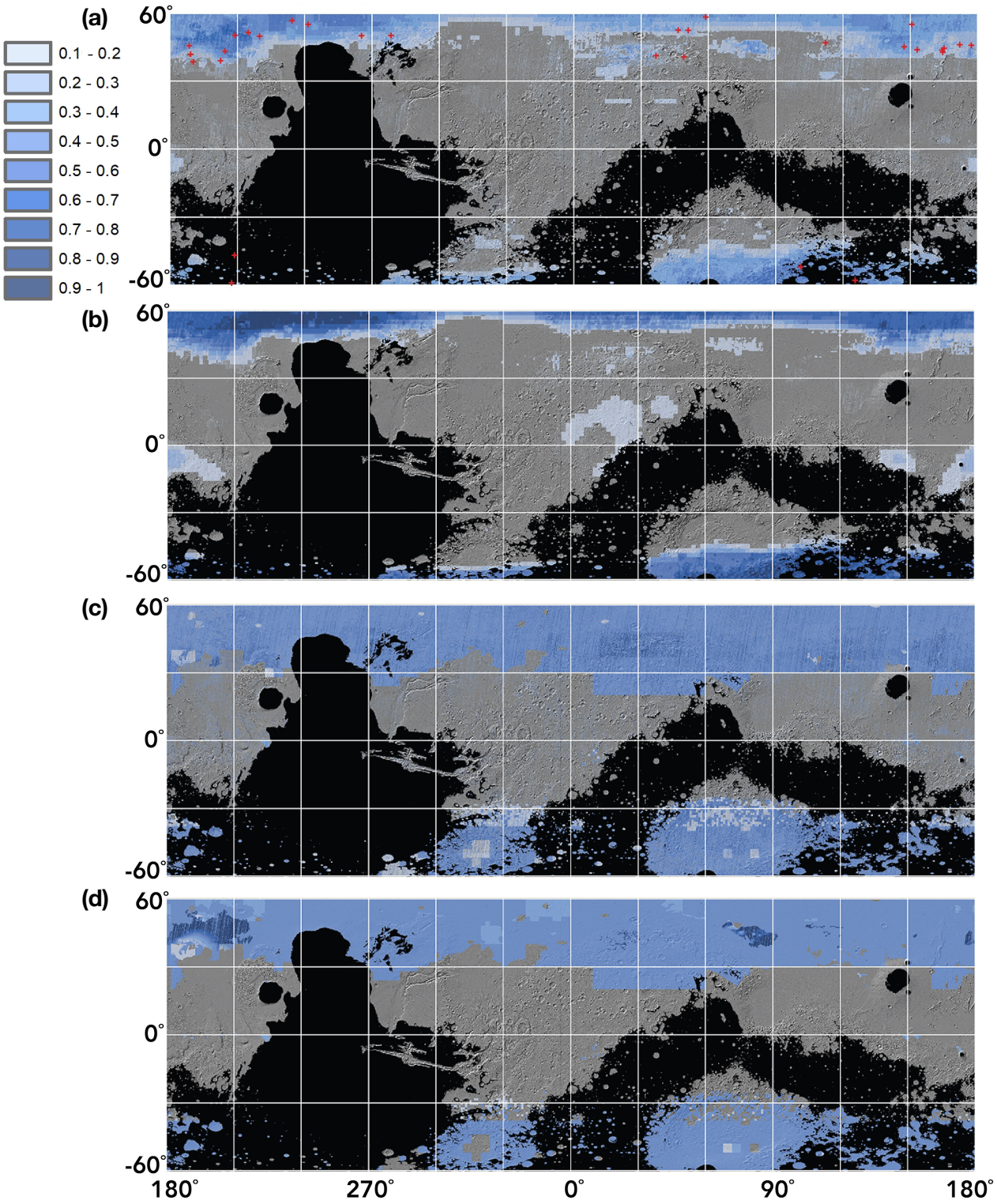

Figure 18.3.1: *Composite ice-consistency maps. (a) For all depths (C_i) using Eq. 1. (b) For depth zone < 1 m (C_i [< 1 m]) using Eq. 2. (c) For depth zone 1–5 m (C_i [1–5 m]) using Eq. 3. (d) For depth zone > 5 m (C_i [> 5 m]) using Eq. 4. Basemaps are MOLA shaded relief, with black masking of elevations above +1 km. Red crosses in (a) represent ice-exposing impacts.*

3.4.Ice consistency for depths greater than 5 meters

We present the results of our predicted ice consistency for depths greater than 5 m in **Fig. 18.3.1d**. Ice consistency in this depth range is driven only by the deep radar and deep geomorphology terms (Eq. 4), since the other terms all have sensing depths ≤ 5 m. The deep geomorphology term excludes mantled and textured terrains due their typical thickness < 5 m, especially at the most equatorward locations where mantle appears as isolated patches and highly dissected. The mapping results for this depth zone are similar in spatial extent to those for C_i [1–5 m] (**Fig. 18.3.1c**) with notable exceptions in the occurrences of the highest ice-consistency values. The deep radar term includes detections of subsurface reflectors associated with widespread units in Arcadia Planitia and Utopia Planitia and glacial landforms across the northern and southern latitudes. The permittivities calculated from these reflectors and their elevation constraints show high consistency with ice. Combined with the corresponding presence of periglacial and glacial landforms, these yield the highest ice consistency in the map (**Fig. 18.3.1d**). The northeast-to-southwest gradient of ice consistency in Arcadia Planitia is likely an artifact of the limited number of elevation tie points available for calculating dielectric permittivity values from radar data in this region.

The excursions of moderate ice consistency into regions < 30° latitude are still present (**Fig. 18.3.1d**) and are due to the occurrences of glacial landforms extending to these latitudes. These glacial landforms appear mostly as isolated CCF or other “icy” fill confined within craters. Unfortunately, the small size of these craters relative to the SHARAD radar footprint limits the ability to detect subsurface reflectors due to the pervasive clutter resulting from the steep crater walls.

Radar reflectors are not observed in many locations where there is geomorphic evidence of ice. Their absence may be due to several factors, including a potential lack of dielectric contrast between ice and regolith, strong attenuation of the radar signal (e.g., from surface roughness), limitations of the vertical and horizontal resolutions of SHARAD radar data, and obscuration of reflectors by clutter. Reflectors are most prevalent in association with LDA, LVF, and CCF in Deuteronilus and Protonilus Mensae and in eastern Hellas, as well as in the Amazonian units in Utopia and Arcadia, resulting in high C_i [> 5 m] values, where subsurface ice may be thickest and/or most pure.

3.5.SWIM Products

All products from the Mars SWIM projects are being made available via the publicly accessible website at https://swim.psi.edu. The team also intends to archive the products with NASA’s Planetary Data System. The website contains PNG, TIFF, and GeoTIFF versions of all the composite C_i maps presented here as well as of dataset-specific ice-consistency maps that went into creating the composites. Other information and ancillary data are also available, such as a map of the depth to the base of ice produced from SHARAD subsurface data.

4.Discussion

4.1.Comparison of SWIM Results to Ice Exposing Impacts

As was discussed in **§18.2.3**, a major challenge to producing synthesized maps of ice presence on Mars is the lack of sufficient ground-truth data with which to calibrate our data products.

Nevertheless, the detection of ice-exposing fresh impacts across Mars (Byrne et al., 2009; Dundas et al, 2014; 2021) provides an opportunity to evaluate our mapping approach.

The first fresh impact to be recognized on Mars was identified in Mars Orbiter Camera (MOC) data (Malin et al., 2006). Since the arrival of MRO to Mars, CTX has been actively employed to search for new impacts. To determine the validity of the detections, each potential impact is followed up by at least one HiRISE observation. With an order-of-magnitude higher resolution relative to CTX and a multi-channel capability (one infrared and two visible color channels), HiRISE enables a search for evidence of ice excavated by the impact (either within the crater or in its ejecta blanket).

During the 2019 phase of the SWIM project, 14 ice-exposing impact sites had been identified within the northern hemisphere study area (**Fig. 18.2.1**) (Dundas et al., 2014). Comparisons between the impact locations and the corresponding values on the ice-consistency map of Morgan et al. (2021) showed good agreement, with 13 of the sites registering positive C_i values. The average C_i value of map pixels containing impacts was 0.26 ± 0.16 and the single negative value was close to zero, and thus considered negligible. As of the publication of Dundas et al. (2021), CTX and HiRISE have identified 48 fresh ice-exposing impact sites within the mid- and high latitudes of Mars, and 30 of these sites are located within the SWIM study region. Comparing the location of these sites with the updated 2020 SWIM mapping using Eq.1 (**Fig. 18.3.1a**; to be concordant with the 2019 analysis), we found that all of the impact sites are within positive C_i pixels that have a mean value of 0.29 ± 0.14.

At most of these sites, there are multiple craters due to bolide break-up in the Martian atmosphere prior to impacting the surface. Regardless of the number of craters at a given site, the diameters of the majority of the ice-exposing impacts are <10 m, with the largest at 48 m. From empirical studies of the relationship between the diameter and depth of impact craters, we expect most of the ice to have been excavated from the upper ~1 m of the subsurface (Dundas et al., 2021). As a result, the ice sampled by the impacts is most relevant to C_i [< 1 m] map product (**Fig. 18.3.1b**). In this case, 27 of the 30 impacts correspond to positive C_i [< 1 m] values, with a mean of 0.39 ± 0.32. One of the three impacts with negative C_i [< 1 m] values is the largest of the ice-exposing impacts with a diameter of 48 m that likely excavated ~4 m into the subsurface. It is therefore possible that the upper meter of the subsurface at this location is ice-free. The corresponding C_i [1–5 m] value for this location, +0.5, is consistent with the presence of deeper ice.

The strong correlation between ice-exposing impacts and the SWIM maps lends weight to the effectiveness of integrating multiple datasets. Within the northern hemisphere, the clustering of low-latitude impacts within longitudes that correspond to broad regions of elevated C_i values (140–220°E) provides further encouragement. It is important to note that a hemispherical discrepancy exists between the number of ice-exposing craters observed in the north relative to the south. The distinct lack of fresh crater detections (icy or not) in the south is likely an observation bias in part related to the lower dust cover (Dundas et al., 2021) and should therefore not be attributed to a lack of buried ice. Additionally, imaging of the clusters of craters indicates that there are local-scale variations in the depth to and concentration of buried ice (Dundas et al., 2021).

4.2.Constraints on Ice Content

To enable the use of buried ice as a resource at any given location, one must understand its geographic distribution, thickness, depth of burial, and purity. The results of the SWIM study contribute to this understanding and place important constraints on each of these factors. A key result is new, more complete mapping of the geographic distribution of where ice is mostly likely to be found. Where subsurface radar returns related to buried ice are constrained by elevation data, they have allowed us to not only determine the depth to the base of ice but also to assess the bulk concentration of ice within the column extending to the surface. Where ice is shallow, the neutron and thermal spectrometer data allowed an estimation of the burial depth within the upper meter of the subsurface, with the neutron data also placing limits on the concentration of the ice. Detection of hydrogen via neutron-spectrometer data is inherently limited to a sensing depth less than about 0.5 m below the Martian surface. Similarly, the ability to detect buried ice by its thermal effects is also limited to about 0.5 m by the thermal skin depth of geologic materials that form the overburden above the ice table. While the SHARAD surface-return data enable some measure of material properties in the upper 5 m, that assessment is of bulk properties and does not allow one to identify variations or distinct interfaces in this zone. The subsurface radar sounding by SHARAD cannot resolve interfaces shallower than 15 m deep due to a combination of the inherent vertical resolution of the radar and its band-limited nature that leads to interferences with the surface return. These considerations leave some shortcomings in our ability to resolve ice content between depths of 0.5 m and 15 m, although the radar surface return does contribute toward understanding properties down to 5 m depth.

4.3.Future Considerations

As noted above, a primary motivation for the SWIM project has been mapping of buried water ice that may serve as a potential resource for future human missions. While the work presented here represents a major advancement in the integration of datasets and their broad application across Mars, there is much more that can be done with the existing data to further evaluate the resource potential of buried ice. For example, due to the practical limitations of time and personnel available for this study, the grid-mapping technique employed did not yield an exhaustive catalog of individual geomorphological indicators of buried ice. More generally, complete mapping at the highest resolutions of all available data was beyond the scope of the project. In addition, a complete scientific assessment of the analyzed data, such as the age, nature and climatological implications of the mapped buried ice, was not part of the funded effort, and the Bayesian statistical approach was limited to a preliminary analysis. The products of this study are intended to guide choices for more in-depth studies by future workers to support their evaluation of potential human landing sites. The SWIM products and methods may also serve to inform future scientific studies related to Martian climate history.

Given the limitations of the currently available data (see **§18.4.2**), obtaining a more thorough understanding of buried ice on Mars will also require new instrumentation. The gap in sensing depth between existing radar and other methods is especially limiting, as one cannot confidently map the depth of the ice table where it extends to depths greater than 0.5 m using currently available data. To resolve these depths, new instrumentation that can build on the capabilities of previous and current instruments is needed. From a global perspective, a high-frequency radar sounder (L–P band) and/or synthetic-aperture radar imager would be extremely complimentary to SWIM and other ice-detection studies by bridging the gap between thermal and neutron

spectroscopy data and the SHARAD data. In this regard the initial plans for an International Mars Ice Mapper (I-MIM) mission (Watzin, 2021) are particularly timely. Ultimately, it would be best to obtain actual ground truth at a prospective human landing site using a landed robotic mission with a drilling system capable of reaching ice within a few meters of the surface.

5.Acknowledgements

The SWIM project was funded by NASA through JPL subcontracts 1589197, 1595721, 1611855, and 1639821. The authors are grateful to NASA, the Italian Space Agency, and the Mars Reconnaissance Orbiter Project for their ongoing support of the MRO mission, which has been invaluable to the work described here. We thank Joseph MacGregor, Laszlo Kestay, Timothy Titus, Kevin Jones, and an anonymous reviewer for insightful comments and suggestions that greatly improved the manuscript.

6.Acronyms and Mathematical Symbols

ATI	Apparent thermal inertia
BF08	Bandfield & Feldman (2008)
c	Speed of light in vacuum
c_h	Bulk heat capacity
C	Ice consistency
C_i	Ice consistency
C_G	Ice consistency derived from geomorphological data
C_{GD}	Ice consistency derived from deep geomorphological data
C_{GS}	Ice consistency derived from shallow geomorphological data
C_N	Ice consistency derived from neutron spectrometer data
C_{RD}	Ice consistency derived from radar subsurface dielectric estimations
C_{RS}	Ice consistency derived from radar surface returns
C_T	Ice consistency derived from thermal spectrometer data
CTX	Context Camera on MRO
CRISM	Compact Reconnaissance Imaging Spectrometer for Mars on MRO
d	Depth below surface
f_i	Volume fraction of ice
f_p	Volume fraction of pore space
f_r	Volume fraction of rock
f_h	Volume fraction of hydrated minerals within rock

h	Thickness (height) of a geologic layer
HiRISE	High Resolution Imaging Science Experiment on MRO
I-MIM	International Mars Ice Mapper
JPL	Jet Propulsion Laboratory
k	Bulk conductivity
LDA	Lobate Debris Apron
L_S	Season (areocentric longitude of the Sun) of buried ice insensitivity
MARSIS	Mars Advanced Radar for Subsurface and Ionospheric Sounding on Mars Express
MCS	Mars Climate Sounder on MRO
MGS	Mars Global Surveyor
MOLA	Mars Orbiter Laser Altimeter on MGS
MONS	Orbiter Neutron Spectrometer on Mars Odyssey
MRO	Mars Reconnaissance Orbiter
NASA	National Aeronautics and Space Administration
NPLD	North polar layered deposits
PDF	Probability density function
pf	Periglacial feature
PQ19	Piqueux et al. (2019)
s_Y	Shallowness of method Y (subscripts as for C_Y listed above)
SP20	SWIM Project (2020)
SPLD	South polar layered deposits
SHARAD	Shallow Radar on MRO
SWIM	Subsurface Water Ice Mapping
TES	Thermal Emission Spectrometer on MGS
TI	Thermal inertia
WEH	Water Equivalent Hydrogen
W_{dn}	WEH weight fraction of a lower (“down”) model layer
W_{up}	WEH weight fraction of an upper model layer
W_{hmax}	Maximum WEH for a subsurface composed of the most hydrated mineral
Δt	Radar two-way delay time

ε'	Real part of the relative permittivity
ε_{eff}	Effective permittivity
ε_i	Ice permittivity
ε_p	Pore-space permittivity
ε_r	Rock permittivity
ρ	Bulk density
ρ_i	Ice density
ρ_r	Rock density
ρ_w	Water density

7.References

Ash, R.L., Dowler, W.L., Varsi, G., 1978. Feasibility of rocket propellant production on Mars. Acta Astronautica 5, 705–724. https://doi.org/10.1016/0094-5765(78)90049-8

Baker, D.M.H., Carter, L.M., 2019. Probing supraglacial debris on Mars 2: Crater morphology. Icarus 319, 264–280. https://doi.org/10.1016/j.icarus.2018.09.009

Bandfield, J. L., Feldman, W. C., 2008. Martian high latitude permafrost depth and surface cover thermal inertia distributions. *J. Geophys. Res. Planets,* 113, https://doi.org/10.1029/2007JE003007

Berman, D.C., Chuang, F.C., Smith, I.B., Crown, D.A., 2021. Ice-rich landforms of the southern mid-latitudes of Mars: A case study in Nereidum Montes. Icarus 355, 114170. https://doi.org/10.1016/j.icarus.2020.114170

Bramson, A.M., Byrne, S., Putzig, N.E., Sutton, S., Plaut, J.J., Brothers, T.C., Holt, J.W., 2015. Widespread excess ice in Arcadia Planitia, Mars. Geophys. Res. Lett 42, 6566–6574. https://doi.org/10.1002/2015GL064844

Brouet, Y., Becerra, P., Sabouroux, P., Pommerol, A., Thomas, N., 2019. A laboratory-based dielectric model for the radar sounding of the martian subsurface. Icarus 321, 960–973. https://doi.org/10.1016/j.icarus.2018.12.029

Byrne, S., Dundas, C.M., Kennedy, M.R., Mellon, M.T., McEwen, A.S., Cull, S.C., Daubar, I.J., Shean, D.E., Seelos, K.D., Murchie, S.L., 2009. Distribution of mid-latitude ground ice on Mars from new impact craters. Science 325, 1674–1676.

Campbell, M. J., & Ulrichs, J.,1969. Electrical properties of rocks and their significance for lunar radar observations. Journal of Geophysical Research, 74, 5867–5881. https://doi.org/10.1029/JB074i025p05867

Campbell, B.A., Putzig, N.E., Carter, L.M., Morgan, G.A., Phillips, R.J., Plaut, J.J., 2013. Roughness and Near−Surface Density of Mars from SHARAD Radar Echoes. J. Geophys. Res. 118, 436–450. https://doi.org/10.1002/jgre.20050

Carr, M.H., 2001. Mars Global Surveyor observations of Martian fretted terrain. J. Geophys. Res. 106, 23571–23593. https://doi.org/10.1029/2000JE001316

Choudhary, P., Holt, J. W., & Kempf, S. D., 2016. Surface Clutter and Echo Location Analysis for the Interpretation of SHARAD Data From Mars. IEEE Geoscience and Remote Sensing Letters, 13(9), 1285–1289. https://doi.org/10.1109/LGRS.2016.2581799

Christensen, P.R., Bandfield, J.L., Hamilton, V.E., Ruff, S.W., Mehall, G.L., Gorelick, N., Bender, K., Murray, K., Kieffer, H.H., Titus, T.N., 2001. Mars Global Surveyor Thermal Emission Spectrometer experiment: Investigation description and surface science results. J. Geophys. Res. 106, 23823–23871.

Dickson, J. L., Kerber, L. A., Fassett, C. I. & Ehlmann, B. L., 2018. A global, blended CTX mosaic of Mars with vectorized seam mapping: a new mosaicking pipeline using principles of non-destructive image editing. In Proc. 49th Lunar and Planetary Science Conference abstr. 2480.

Dundas, C.M., Byrne, S., 2010. Modeling sublimation of ice exposed by new impacts in the martian mid-latitudes. Icarus 206, 716–728. https://doi.org/10.1016/j.icarus.2009.09.007

Dundas, C.M., Byrne, S., McEwen, A.S., Mellon, M.T., Kennedy, M.R., Daubar, I.J., Saper, L., 2014. HiRISE observations of new impact craters exposing Martian ground ice. J. Geophys. Res. 119, 109–127. https://doi.org/10.1002/2013JE004482

Dundas, C.M., Bramson, A.M., Ojha, L., Wray, J.J., Mellon, M.T., Byrne, S., McEwen, A.S., Putzig, N.E., Viola, D., Sutton, S., Clark, E., Holt, J.W., 2018. Exposed subsurface ice sheets in the Martian mid-latitudes. Science 359, 199–201. https://doi.org/10.1126/science.aao1619

Dundas, C.M., Mellon, M.T., Conway, S.J., Daubar, I.J., Williams, K.E., Ojha, L., Wray, J.J., Bramson, A.M., Byrne, S., McEwen, A.S., Posiolova, L.V., Speth, G., Viola, D., Landis, M.E., Morgan, G.A., Pathare, A.V., 2021. Widespread Exposures of Extensive Clean Shallow Ice in the Mid−Latitudes of Mars. J Geophys Res Planets. https://doi.org/10.1029/2020JE006617

Feldman, W.C., Boynton, W.V., Tokar, R.L., Prettyman, T.H., Gasnault, O., Squyres, S.W., Elphic, R.C., Lawrence, D.J., Lawson, S.L., Maurice, S., McKinney, G.W., Moore, K.R., Reedy, R.C., 2002. Global distribution of neutrons from Mars: Results from Mars Odyssey. Science 297, 75–78. https://doi.org/10.1126/science.1073541

Feldman, W.C., Pathare, A., Maurice, S., Prettyman, T.H., Lawrence, D.J., Milliken, R.E., Travis, B.J., 2011. Mars Odyssey neutron data: 2. Search for buried excess water ice deposits at nonpolar latitudes on Mars. *Journal of Geophysical Research: Planets*, 116(E11).

Grima, C., Kofman, W., Mouginot, J., Phillips, R.J., Hérique, A., Biccari, D., Seu, R., Cutigni, M., 2009. North polar deposits of Mars: Extreme purity of the water ice. Geophys. Res. Lett. 36, L03203, doi:10.1029/2008GL036236, 4 p.

Grima, C., Kofman, W., Herique, A., Orosei, R., Seu, R., 2012. Quantitative analysis of Mars surface radar reflectivity at 20MHz. Icarus 220, 84–99.

Head, J.W., Marchant, D.R., Dickson, J.L., Kress, A.M., Baker, D.M., 2010. Northern mid-latitude glaciation in the Late Amazonian period of Mars: Criteria for the recognition of debris-covered glacier and valley glacier landsystem deposits. Earth and Planetary Science Letters 294, 306–320. https://doi.org/10.1016/j.epsl.2009.06.041

Kadish, S.J., Barlow, N.G., Head, J.W., 2009. Latitude dependence of Martian pedestal craters: Evidence for a sublimation-driven formation mechanism. J. Geophys. Res. 114, E10001. https://doi.org/10.1029/2008JE003318

Kieffer, H. H., 2013. Thermal model for analysis of Mars infrared mapping. *J. Geophys. Res. Planets,* 118, 451-470.

Koledintseva, M. et al., 2006. “A Maxwell Garnett Model for Dielectric Mixtures Containing Conducting Particles at Optical Frequencies.” *Progress in Electromagnetics Research* 63, 223-242.

Kostama, V.-P., Kreslavsky, M.A., Head, J.W., 2006. Recent high-latitude icy mantle in the northern plains of Mars: Characteristics and ages of emplacement. Geophys. Res. Lett. 33, L11201. https://doi.org/10.1029/2006GL025946

Kress, A.M., Head, J.W., 2008. Ring-mold craters in lineated valley fill and lobate debris aprons on Mars: Evidence for subsurface glacial ice. Geophys. Res. Lett. 35, L23206. https://doi.org/10.1029/2008GL035501

Leighton, R.B., Murray, B.C., 1966. Behavior of carbon dioxide and other volatiles on Mars. Science 153, 136–144.

Levy, J.S., Fassett, C.I., Head, J.W., Schwartz, C., Watters, J.L., 2014. Sequestered glacial ice contribution to the global Martian water budget: Geometric constraints on the volume of remnant, midlatitude debris-covered glaciers: Buried martian glaciers. J. Geophys. Res. Planets 119, 2188–2196. https://doi.org/10.1002/2014JE004685

Malakhov, A.V., Mitrofanov, I.G., Litvak, M.L., Sanin, A.B., Golovin, D.V., Djachkova, M.V., Nikiforov, S.Yu., Anikin, A.A., Lisov, D.I., Lukyanov, N.V., Mokrousov, M.I., 2020. Ice Permafrost ‘“Oases”’ Close to Martian Equator: Planet Neutron Mapping Based on Data of FREND Instrument Onboard TGO Orbiter of Russian-European ExoMars Mission. Astron. Lett. 46, 407–421. https://doi.org/10.1134/S1063773720060079

Malin, M.C., Edgett, K.S., Posiolova, L.V., McColley, S.M., Dobrea, E.Z.N., 2006. Present-Day Impact Cratering Rate and Contemporary Gully Activity on Mars. Science 314, 1573–1577. https://doi.org/10.1126/science.1135156

Mangold, N., 2005. High latitude patterned grounds on Mars: Classification, distribution and climatic control. Icarus 174, 336–359.

Mellon, M. T., Jakosky, B. M., Postawko, S. E., 1997. The persistence of equatorial ground ice on Mars. *J. Geophys. Res.,* 102, 19357-19369.

Mellon, M. T., Jakosky, B. M., Kieffer, B. M., Kieffer, H. H., Christensen, P. R., 2000. High-Resolution Thermal Inertia Mapping from the Mars Global Surveyor Thermal Emission Spectrometer. *Icarus,* 148, 437-455.

Mellon, M. T., Feldman, W. C., Prettyman, T. H., 2004. The presence and stability of ground ice in the southern hemisphere of Mars. *Icarus,* 169, 324-340.

Milliken, R.E., Mustard, J.F., Goldsby, D.L., 2003. Viscous flow features on the surface of Mars: Observations from high-resolution Mars Orbiter Camera (MOC) images. J. Geophys. Res. 108, 5057. https://doi.org/10.1029/2002JE002005

Morgan, G. A., Campbell, B. A., 2017. Local Subsurface Ice Mapping Through the Integration of SHARAD Derived Data Products with Other Datasets: A proposal to the Jet Propulsion Laboratory Request for Proposals No: KM-2691-947266 on Mapping of Water Deposits to Support NASA Mars Exploration Program Studies.

Morgan,G. A., Putzig, N. E., Perry, M. R., Sizemore, H. G., Bramson, A. M., Petersen, E. I., Bain, Z. M., Baker, D. M. H., Mastrogiuseppe, M., Hoover, R. H., Smith,I. B., Pathare, A., Dundas, C. M., Campbell, B. A., 2021. Availability of Martian Water-Ice Resources to Support Human Missions. *Nature Astronomy.* https://doi.org/10.1038/s41550-020-01290-z

Morgenstern, A., Hauber, E., Reiss, D., van Gasselt, S., Grosse, G., Schirrmeister, L., 2007. Deposition and degradation of a volatile-rich layer in Utopia Planitia and implications for climate history on Mars. J. Geophys. Res. 112, E06010. https://doi.org/10.1029/2006JE002869

Mouginot, J., Pommerol, A., Kofman, W., Beck, P., Schmitt, B., 2010. The 3-5 MHz global reflectivity map of Mars by MARSIS/Mars Express: implications for the current inventory of subsurface H2O. *Icarus* 210, 612-625.

Mustard, J.F., Cooper, C.D., Rifkin, M.K., 2001. Evidence for recent climate change on Mars from the identification of youthful near-surface ground ice. Nature 412, 411–414.

Pathare, A.V., Feldman, W.C., Prettyman, T.H., Maurice, S., 2018. Driven by excess? Climatic implications of new global mapping of near-surface water-equivalent hydrogen on Mars. *Icarus* 301, 97–116. https://doi.org/10.1016/j.icarus.2017.09.031

Petersen, E. I., Holt, J. W., & Levy, J. S., 2018. High Ice Purity of Martian Lobate Debris Aprons at the Regional Scale: Evidence From an Orbital Radar Sounding Survey in Deuteronilus and Protonilus Mensae. Geophysical Research Letters, 45(21), 11,595-11,604. https://doi.org/10.1029/2018GL079759

Piqueux, S., Christensen, P. R., 2009. A model of thermal conductivity for planetary soils 2. Theory for cemented soils. *J. Geophys. Res,* 114, doi: 10.1029/2008JE003309.

Piqueux, S., Buz, J., Edwards, C. S., Bandfield, J. L., Kleinböhl, A., Kass, D. M., Hayne, P. O., and the MCS and THEMIS Teams, 2019. Widespread shallow water ice on Mars at high latitudes and midlatitudes. *Geophys. Res. Let.,* 46, 14290–14298.

Plaut, J.J., Ivanov, A., Safaeinili, A., Milkovich, S.M., Picardi, G., Seu, R., Phillips, R., 2007. Radar sounding of subsurface layers in the south polar plains of Mars: Correlation with the Dorsa Argentea Formation. Presented at the Lunar Planet. Sci.

Putzig, N.E., Mellon, M.T., 2007. Apparent thermal inertia and the surface heterogeneity of Mars. Icarus 191, 68–94. https://doi.org/10.1016/j.icarus.2007.05.013

Putzig, N. E., Barratt, E. M., Mellon, M. T., Michaels, T. I., 2013. MARSTHERM: A Web-based System Providing Thermophysical Analysis Tools for Mars Research. AGU Fall Meeting, abstract P43C-2023

Putzig, N. E., Mellon, M. T., Herkenhoff, K. E., Phillips, R. J, Davis, B. J., Ewer, K. J., Bowers, L. M., 2014. Thermal behavior and ice-table depth within the north polar erg of Mars. *Icarus,* 230, 64-76.

Putzig, N. E., Sizemore, H. G., Smith, I. B., 2017. Mapping Buried Water Ice in Arcadia & Beyond with Radar & Thermal Data: A proposal to the Jet Propulsion Laboratory Request for Proposals No: KM-2691-947266 on Mapping of Water Deposits to Support NASA Mars Exploration Program Studies.

Ramsdale, J.D., Balme, M.R., Conway, S.J., Gallagher, C., van Gasselt, S.A., Hauber, E., Orgel, C., Séjourné, A., Skinner, J.A., Costard, F., Johnsson, A., Losiak, A., Reiss, D., Swirad, Z.M., Kereszturi, A., Smith, I.B., Platz, T., 2017. Grid-based mapping: A method for rapidly determining the spatial distributions of small features over very large areas. Planet. Space Sci. 140, 49–61. https://doi.org/10.1016/j.pss.2017.04.002

Seu, R., Phillips, R.J., Biccari, D., Orosei, R., Masdea, A., Picardi, G., Safaeinili, A., Campbell, B.A., Plaut, J.J., Marinangeli, L., Smrekar, S.E., Nunes, D.C., 2007. SHARAD sounding radar on the Mars Reconnaissance Orbiter. J. Geophys. Res. 112, E05S05. https://doi.org/10.1029/2006JE002745

Shean, D.E., 2010. Candidate ice-rich material within equatorial craters on Mars. Geophys. Res. Lett. 37, L24202. https://doi.org/10.1029/2010GL045181

Siegler, M., Aharonson, O., Carey, E., Choukroun, M., Hudson, T., Schorghofer, N., Xu, S., 2012. Measurements of thermal properties of icy Mars regolith analogs. *J. Geophys. Res. Planets,* 117, https://doi.org/10.1029/2011JE003938.

Sihvola, A. H., 1999. Electromagnetic Mixing Formulas and Applications. London, UK. Institution of Electrical Engineers, Electromagnetic Waves Series 47.

Smith, P.H., Tamppari, L., Arvidson, R.E., Bass, D., Blaney, D., Boynton, W., Carswell, A., Catling, D., Clark, B., Duck, T., DeJong, E., Fisher, D., Goetz, W., Gunnlaugsson, P., Hecht, M., Hipkin, V., Hoffman, J., Hviid, S., Keller, H., Kounaves, S., Lange, C.F., Lemmon, M., Madsen, M., Malin, M., Markiewicz, W., Marshall, J., McKay, C., Mellon, M., Michelangeli, D., Ming, D., Morris, R., Renno, N., Pike, W.T., Staufer, U., Stoker, C., Taylor, P., Whiteway, J., Young, S., Zent, A., 2008. Introduction to special section on the Phoenix Mission: Landing Site Characterization Experiments, Mission Overviews, and Expected Science. J. Geophys. Res. 113, E00A18. https://doi.org/10.1029/2008JE003083

Souness, C., Hubbard, B., 2012. Mid-latitude glaciation on Mars. Progress in Physical Geography: Earth and Environment 36, 238–261. https://doi.org/10.1177/0309133312436570

Stillman, D. E., Grimm, R. E., & Dec, S. F., 2010. Low-Frequency Electrical Properties of Ice−Silicate Mixtures. The Journal of Physical Chemistry B, 114(18), 6065–6073. https://doi.org/10.1021/jp9070778

Tanaka, K.L., Skinner, J.A., Hare, T.M., 2005. Geologic map of the northern plains of Mars, USGS Scientific Investigations Map 2888. US Geological Survey.

Tarantola, Albert, 2005. Inverse problem theory and methods for model parameter estimation. Society for Industrial and Applied Mathematics.

Ulaby, F.T., Moore, R.K. and Fung, A.K., 1986. Microwave Remote Sensing: Active and Passive. Vol. 2. Radar Remote Sensing and Surface Scattering and Emission Theory. Ch. 12, Artech House Publishers, Norwood, 962-966.

Viola, D., McEwen, A.S., Dundas, C.M., Byrne, S., 2015. Expanded secondary craters in the Arcadia Planitia region, Mars: Evidence for tens of Myr-old shallow subsurface ice. Icarus 248, 190–204.

Viola, D., McEwen, A.S., 2018. Geomorphological Evidence for Shallow Ice in the Southern Hemisphere of Mars. J. Geophys. Res. Planets 123, 262–277. https://doi.org/10.1002/2017JE005366

Watzin, J., 2021. NASA Perspectives on future exploration science at Mars. Presentation to the Mars Exploration Program Analysis Group (MEPAG), Virtual Meeting 11, January 27.

Wilson, J.T., Eke, V.R., Massey, R.J., Elphic, R.C., Feldman, W.C., Maurice, S., Teodoro, L.F.A., 2018. Equatorial locations of water on Mars: Improved resolution maps based on Mars Odyssey Neutron Spectrometer data. Icarus 299, 148–160. https://doi.org/10.1016/j.icarus.2017.07.028

Zubrin, R., Daker, D., Gwynne, O., 1991. Mars direct: a simple, robust, and cost effective architecture for the Space Exploration Initiative. In Proc. 29th Aerospace Sciences Meeting, AIAA.